


RESEARCH ARTICLE | AUGUST 29 2023

Phase-field simulations of polarization variations in polycrystalline $\text{Hf}_{0.5}\text{Zr}_{0.5}\text{O}_2$ based MFIM: Voltage dependence and dynamics

Revanth Koduru ; Imtiaz Ahmed ; Atanu K. Saha ; Xiao Lyu ; Peide Ye ; Sumeet K. Gupta 

 Check for updates

J. Appl. Phys. 134, 084104 (2023)

<https://doi.org/10.1063/5.0158997>


View Online


Export Citation

CrossMark

starting at
EUR 6,360,-



Grows with your experiment.
The MFLI Lock-in Amplifier.

Field-upgradeable options

- 5 MHz frequency extension
- Multi-frequency analysis
- PID controller
- Impedance analyzer

 Zurich Instruments [Find out more](#)

Phase-field simulations of polarization variations in polycrystalline $\text{Hf}_{0.5}\text{Zr}_{0.5}\text{O}_2$ based MFIM: Voltage dependence and dynamics

Cite as: J. Appl. Phys. 134, 084104 (2023); doi: 10.1063/5.0158997

Submitted: 19 May 2023 · Accepted: 4 August 2023 ·

Published Online: 29 August 2023



Revanth Koduru,^{a)} Imtiaz Ahmed, Atanu K. Saha, Xiao Lyu, Peide Ye, and Sumeet K. Gupta

AFFILIATIONS

Elmore Family School of Electrical and Computer Engineering, Purdue University, West Lafayette, Indiana 47906, USA

^{a)}Author to whom correspondence should be addressed: kodurur@purdue.edu

ABSTRACT

In this work, we investigate the device-to-device variations in the remanent polarization of metal–ferroelectric–insulator–metal stacks based on ferroelectric hafnium–zirconium–oxide (HZO). Our study employs a 3D dynamic multi-grain phase-field model to consider the effects of the polycrystalline nature of HZO in conjunction with the multi-domain polarization switching. We explore the dependence of variations on various design factors, such as the ferroelectric thickness and voltage stimuli (set voltage, pulse amplitude, and width), and correlate the trends to the underlying polarization switching mechanisms. Our analysis reveals a non-monotonic dependence of variations on the set voltage due to the coupled effect of the underlying polycrystalline structure variations and the voltage dependence of polarization switching mechanisms. We further report that collapsing of oppositely polarized domains at higher set voltages can lead to an increase in variations, while ferroelectric thickness scaling lowers the overall device-to-device variations. Considering the dynamics of polarization switching, we highlight the key role of voltage and temporal dependence of domain nucleation in dictating the trends in variations. Finally, we show that using a lower amplitude pulse for longer duration to reach a target mean polarization state results in lower variations compared to using a higher amplitude pulse for shorter duration.

Published under an exclusive license by AIP Publishing. <https://doi.org/10.1063/5.0158997>

I. INTRODUCTION

In recent years, ferroelectric devices have gained renewed attention due to the discovery of ferroelectricity in doped hafnium oxide.¹ The CMOS process compatibility² of HfO_2 along with the scale-free nature of its ferroelectricity³ have propelled ferroelectric (FE) devices as potential candidates for future electronics. Researchers have demonstrated multiple flavors of hafnium–zirconium–oxide (HZO)-based ferroelectric (FE) devices, including ferroelectric capacitors, ferroelectric field effects transistors (FEFETs), and ferroelectric tunnel junctions (FTJs). These devices exhibit various appealing attributes^{4–9} such as multilevel operation, stochastic switching, and polarization accumulation making them promising candidates for various emerging and in-demand applications such as non-volatile memories, electronic synapses, and neurons.^{9–14}

However, commercialization of these devices is contingent upon addressing several key material and device-level challenges.^{15–20} Among these, the device-to-device variations^{19–25} resulting from the polycrystalline nature²⁶ of HZO is particularly crucial due to its

significant implications on a wide range of applications.^{20–23} Certainly, optimizing the material properties of HZO via process and material engineering will be the key in addressing the polycrystallinity and improving the stability of the ferroelectric phase.²⁰ Nevertheless, understanding the dependence of the polycrystallinity-induced device-to-device variations on various design knobs and device parameters will be crucial in developing superior design solutions.

Previous studies in this area^{21–25} have investigated various dependencies of polycrystallinity-induced device-to-device variations and proposed multiple device and design-level optimization strategies. For instance, Ni *et al.*²¹ showed an increase in variations in the output current (I_{DS}) characteristics of FEFETs with area scaling. They further demonstrated that using higher pulse amplitudes and longer pulse widths for gate voltage lowers the variations and improves the distinguishability between negative and positive ($-P$ and $+P$) polarization states. Koduru *et al.*²⁵ showed a decrease in the variations of the remanent polarization state in metal–

30 October 2023 15:21:44

ferroelectric–insulator–metal (MFIM) stacks with a reduction in FE thickness. The authors have correlated this trend to the increase in the polarization domain density and reduction in the random domain nucleation process with FE thickness scaling. Furthermore, Ni *et al.*²⁴ examined the impact of variations in parameters of the ferroelectric layer and the underlying transistor in FEFETs and demonstrated that FE parameter variations contribute significantly to the variations in device characteristics (I_{DS}).

These existing studies have predominantly focused on the two-state ($-P$ and $+P$) operation of the FE layer. However, for various applications, such as multi-state memories and neuromimetic devices,^{12,13,27} multi-state ($+P$, $-P$ and intermediate polarization states) operation of FE devices is crucial. In the context of multi-state operation of FEFETs, experiments^{23,28} have shown a non-monotonic dependence of variations in the polarization states on the set or reset voltages. However, the mechanisms responsible for this non-monotonic dependence remain poorly understood. Furthermore, the dependence of variations on the gate voltage parameters such as pulse amplitude and width has not been fully explored for multi-state operation. Moreover, a comprehensive correlation between the device-to-device variations and the underlying polycrystalline structures and polarization switching mechanisms is still lacking. Understanding these dependencies and correlations is crucial as they can provide valuable insights and aid in optimizing the ferroelectric devices for various applications.

In this work, we aim to address these gaps by extensively studying the polycrystallinity-induced device-to-device variations in the MFIM stacks, considering the multi-state operation of the FE layer. To achieve this, we utilize our in-house 3D dynamic multi-grain phase-field simulation framework, which captures the multi-domain polarization switching dynamics along with the polycrystalline nature of HZO as well as the inter- and intra-grain interactions. For this study, we focus on polycrystalline HZO-based Metal–Ferroelectric–Insulator–Metal (MFIM) stacks, as it is a primitive structure across various FE devices. Our analysis centers around understanding the variations in remanent polarization states across the samples, given its central role in determining the distinguishability between different states in FE-based devices. We mainly focus on analyzing the impact of applied voltage (V_{APP}) on the device-to-device variations of the remanent polarization states and correlating the trends to the underlying polarization switching mechanisms and polycrystalline nature of HZO.

Key contributions of this work include

- A thorough analysis of the dependence of device-to-device variations on the set voltage (V_{SET}) considering multi-state polarization retention.
- Investigation of the dependence of the device-to-device variations on voltage pulse parameters, specifically the pulse amplitude (V_{pulse}) and the pulse width (t_{pulse}).
- Presentation of a strategy to achieve a target mean intermediate polarization state across samples with minimal device-to-device variations.
- Correlation of trends in variations to the multi-domain polarization switching mechanisms and the effects of underlying polycrystalline structures.

II. 3D DYNAMIC MULTI-GRAIN PHASE-FIELD SIMULATION FRAMEWORK

Our 3D multi-grain phase-field simulation framework²⁵ [Fig. 1(a)] captures the effects of polycrystalline nature of HZO²⁶ along with the multi-domain formation²⁷ on the polarization switching characteristics of MFIM stacks [Fig. 1(b)]. We achieve this by coupling a 3D grain-growth equation²⁹ that models the polycrystalline structure of HZO, with a 3D phase-field model that simulates the behavior of the MFIM stack subjected to an applied electric field or voltage (V_{APP}).

The 3D grain-growth equation²⁹ models the polycrystalline microstructure using multiple (K) abstract order parameters (η_k) whose evolution follows a time-dependent Ginzburg Landau formalism as

$$\frac{\partial \eta_k(r, t)}{\partial t} = -L(-a\eta_k(r, t) + b\eta_k^3(r, t) + 2c\eta_k(r, t) \sum_{s \neq k}^K \eta_s^2(r, t) - \kappa \nabla^2 \eta_k(r, t)), \quad (1)$$

where the parameters $a = 1$, $b = 1$, $c = 1$, $\kappa = 0.5$, kinetic rate coefficient $L = 1$, and number of order parameters $K = 20$ are calibrated to match the grain diameter distributions of the generated polycrystalline structures to the experimental distributions³⁰ for various HZO film thicknesses. The comparison between the simulated and experimental grain diameter distributions is reported in Koduru *et al.*²⁵

These order parameters (η_k) are then randomly mapped to the grain orientation angles (θ_i)—the angle between the polarization direction (c axis in the orthorhombic crystal phase³¹), of the grain and the physical thickness direction of the HZO film [Fig. 1(d)]. The grain orientation angle (θ_i) serves as the differentiating factor between the grains [Fig. 1(c)], resulting in different polarization directions across them.

To capture this change in polarization direction across the grains, we employ two coordinate systems in our simulation framework: a global coordinate system [$G:(x, y, z)$] and a local coordinate system [$L:(a, b, c)$] [Fig. 1(d)]. The global coordinate system is constant across all the layers of the MFIM stacks with its z axis along the physical thickness direction of the stack. On the other hand, the local coordinate system is defined only in the FE layer and varies from one grain to another, its c axis aligning with the polarization direction of the grain, i.e., c axis makes an angle θ_i with the z axis.

The polarization in each grain of the FE layer is represented as P_c^L , where the superscript L represents the local coordinate system, and the subscript c represents the polarization direction. Similarly, the polarization with respect to global coordinate system is represented as P_x^G . The transformation from the global to local coordinate system is performed using rotation matrix (R_{θ_i}),

$$R_{\theta_i} = \begin{pmatrix} 1 & 0 & 0 \\ 0 & \cos(\theta_i) & -\sin(\theta_i) \\ 0 & \sin(\theta_i) & \cos(\theta_i) \end{pmatrix}. \quad (2)$$

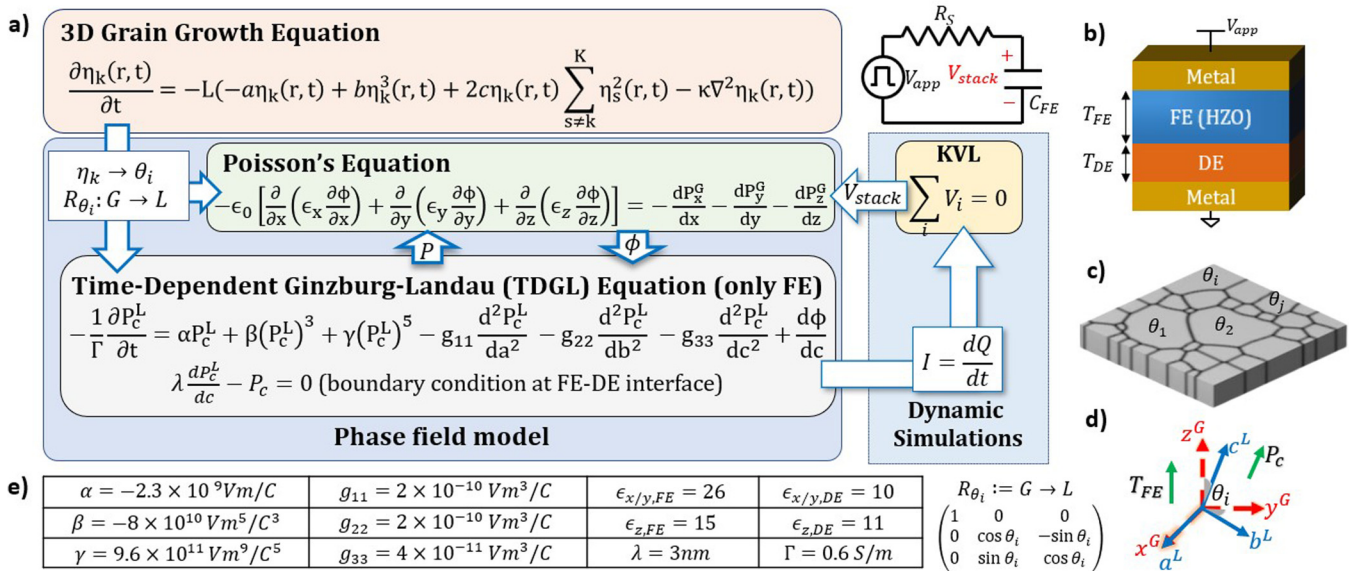


FIG. 1. (a) Dynamic 3D grain-growth coupled phase-field simulation framework (Poisson's + TDGL self-consistently coupled with KVL) considering the equivalent circuit emulating the measurement setup. (b) Metal-Ferroelectric-Insulator-Metal (MFIM) structure. (c) Sample polycrystalline structure generated by 3D grain-growth equation. (d) Two coordinate axes system used in the framework: x-y-z (global) and a-b-c (local). (e) Calibrated parameters used in the simulation framework along with the rotation matrix to relate variable from local to global coordinate systems and vice versa.

The 3D phase-field simulation framework²⁵ [Fig. 1(a)] calculates the potential (ϕ) and polarization (P) profiles of the MFIM stack, taking into account the polycrystalline structures generated by the grain-growth equation for the underlying FE layer. The framework self-consistently solves the Time-dependent Ginzburg Landau (TDGL) and Poisson's equations for a given applied voltage (V_{APP}). These equations are solved in 3D real space employing the finite difference method.

The TDGL equation models the polarization switching behavior of the FE layer. The equation relates the rate of change of polarization (P_c^L) to a thermodynamic force that is dependent on the total energy of the system (F) as in Eq. (3). The TDGL equation is solved on the local coordinate system to accurately capture the change in direction of polarization across the grains,

$$-\frac{1}{\Gamma} \frac{dP_c^L}{dt} = \frac{dF}{dP_c^L}, \quad (3)$$

$$F = f_{free} + f_{elec} + f_{grad},$$

where Γ is the viscosity coefficient. In our phase-field framework, the total energy of the system (F) is divided into free (f_{free}), electrostatic (f_{elec}), and gradient (f_{grad}) energy components. We neglect the contribution of elastic and electrostatic energy components to the total energy of the system due to the assumption of uniform strain across the FE layer.

The free energy (f_{free}) captures the stability of the spontaneous polarization states ($+P$ and $-P$) using a double-well potential with energy barrier separating the two states. In our framework,

the f_{free} is represented using Landau's free energy equation as shown in Eq. (4),

$$f_{free} = \frac{\alpha}{2} (P_c^L)^2 + \frac{\beta}{4} (P_c^L)^4 + \frac{\gamma}{6} (P_c^L)^6, \quad (4)$$

where α , β , and γ are the Landau free energy parameters.

The presence of electric field (E_c) along the c axis resulting from an external applied voltage or imperfect screening of the polarization charges (depolarization field) at the ferroelectric interfaces contributes to the electrostatic energy component represented as

$$f_{elec} = -E_c \cdot P_c. \quad (5)$$

Furthermore, HZO often exhibits multi-domain polarization structure due to various factors, such as polycrystallinity, non-uniform strain, or simply to minimize the depolarization field and the resulting electrostatic energy. This spatial variation in polarization results in an energy cost dependent on the elastic coupling between the unit cells, which is represented by the gradient energy component f_{grad} as

$$f_{grad} = g_{11} \left(\frac{\partial P_c^L}{\partial a} \right)^2 + g_{22} \left(\frac{\partial P_c^L}{\partial b} \right)^2 + g_{33} \left(\frac{\partial P_c^L}{\partial c} \right)^2, \quad (6)$$

where g_{11} , g_{22} , and g_{33} are the gradient energy coefficients. At the FE-DE interface, the surface energy is taken into account

by using Eq. (7),

$$\lambda \frac{\partial P_c^L}{\partial c} - P_c^L = 0, \quad (7)$$

where λ is the screening length.

Substituting these different energy components into the TDGL equation, Eq. (3) results in Eq. (8),

$$-\frac{1}{\Gamma} \frac{\partial P_c^L}{\partial t} = \alpha P_c^L + \beta (P_c^L)^3 + \gamma (P_c^L)^5 - g_{11} \frac{\partial^2 P_c^L}{\partial a^2} - g_{22} \frac{\partial^2 P_c^L}{\partial b^2} - g_{33} \frac{\partial^2 P_c^L}{\partial c^2} + \frac{d\phi}{dc}. \quad (8)$$

Poisson's equation captures the electrostatic behavior of the MFIM system,

$$-\epsilon_0 \left[\frac{\partial}{\partial x} \left(\epsilon_x \frac{\partial \phi}{\partial x} \right) + \frac{\partial}{\partial y} \left(\epsilon_y \frac{\partial \phi}{\partial y} \right) + \frac{\partial}{\partial z} \left(\epsilon_z \frac{\partial \phi}{\partial z} \right) \right] = -\frac{\partial P_x^G}{\partial x} - \frac{\partial P_y^G}{\partial y} - \frac{\partial P_z^G}{\partial z}, \quad (9)$$

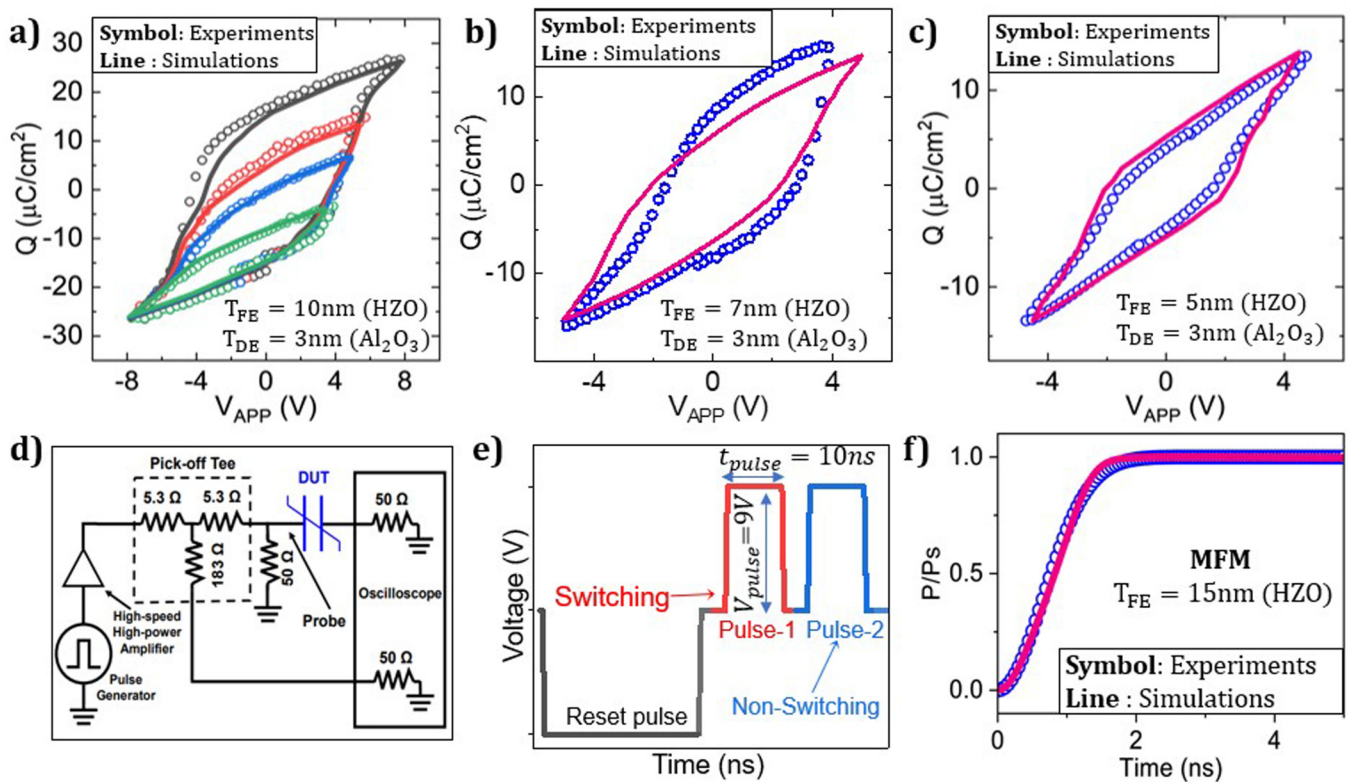
where ϵ_x , ϵ_y , and ϵ_z are the material permittivity values along the x , y , and z directions, respectively. Poisson's equation is solved using the global coordinate system to ensure continuity throughout the entire MFIM stack. We account for the polarization-induced bound charges in the FE layer in Poisson's equation via the terms $\frac{\partial P_x^G}{\partial x}$, $\frac{\partial P_y^G}{\partial y}$, and $\frac{\partial P_z^G}{\partial z}$.

To capture the effect of external circuit elements on the dynamics of polarization switching, we couple the phase-field model with a "Kirchhoff's Voltage Law (KVL)" module [Fig. 1(a)]. The KVL module implements

$$\sum_{i \in \text{nodes}} V_i = 0, \quad (10)$$

considering Thevenin's equivalent [Fig. 1(a)] for the circuit used in the experimental setup [Fig. 2(d)]. Here, V_i represents the potential of node i in Thevenin's equivalent circuit with Thevenin's resistance of R_s and MFIM capacitance of C_{FE} .

At any time step, the total current (I) in the circuit is computed based on the rate of change of the total charge (Q) on the metal plate of the MFIM stack, expressed as $I = dQ/dt$. This total current accounts for various contributions, including currents resulting from



30 October 2023 15:21:44

FIG. 2. Simulated and experimental charge Q vs applied voltage V_{APP} characteristics for the MFIM stack for three different T_{FE} of (a) 10, (b) 7, and (c) 5 nm. (d) Experimental setup³² for dynamic measurements using the PUND technique. (e) Pulse scheme used for the dynamic measurements in experiments³² and (f) simulated and experimental normalized polarization (P/P_s) vs time (t).

ferroelectric polarization switching, background permittivity or dielectric behavior, and displacement current (CdV/dt). It is essential to note here that we do not consider the effect of traps and defects in our model, thereby the current due to trap filling process is not captured. Moreover, our analysis in this work focuses on MFIM stacks with relatively thick ferroelectric (10 nm) and dielectric (3 nm) layers. Given these thicker layers, we make a reasonable assumption to neglect leakage current in our simulation framework. Utilizing the total current (I), the KVL module calculates the voltage across the MFIM stack (V_{stack}). We then pass this voltage (V_{stack}) to the phase-field model, which determines the polarization (P) and potential (ϕ) profiles of the MFIM stack.

To ensure consistency in the temporal evolution of polarization (P), current (I), and potential (ϕ), we solve the phase-field and KVL models in an iterative and self-consistent manner at each time step. The overall simulation framework along with the flow of variables between different modules as well as its self-consistent nature is depicted in Fig. 1(a).

Our framework is distinctive in its ability to capture non-uniform grain shapes and sizes along with inter- and intra-grain interactions, unlike most other models for HZO-based devices. Furthermore, it also captures polarization switching through both domain growth and domain nucleation mechanisms. However, it is important to note that, in our current framework, we make certain assumptions such as the presence of only the orthorhombic phase in the FE layer, similar inter- and intra-grain elastic interactions and uniform strain in the HZO layer. Additionally, we do not consider the effects of traps, defects, and leakage current in our model. While these assumptions will change the magnitude of variations, we expect that the trends in variations that we present (which is the main objective of this paper) and their correlations to the underlying physical mechanisms will hold.

To ensure the accuracy in the trends predicted by our framework, we calibrate the parameters in the TDGL equation and material properties using the experimental results. For this, we fabricate MFIM samples with 3 nm Al_2O_3 dielectric layer and 5, 7, and 10 nm HZO ferroelectric layers. These samples are fabricated using atomic layer deposition (ALD) at 200 °C followed by rapid thermal annealing at 500 °C in an N_2 environment (complete details of the fabrication methodology are presented in Saha *et al.*³³). We then characterize these samples using low-frequency (50 Hz) Q–V measurements to calibrate the material permittivity (ϵ), free energy (α, β, γ), and gradient energy (g_{11}, g_{22}, g_{33}) coefficients of the TDGL equation.

To factor in the device-to-device and cycle-to-cycle variations in the Q–V characteristics, we simulate 20 MFIM samples with different polycrystalline structures for the HZO layer over five voltage cycles and use the average of these simulated characteristics to calibrate with the experimental data. The aforementioned parameters are calibrated for major loop of 10 nm HZO thickness (T_{FE}). These parameters are then validated by simulating the minor loops for $T_{FE} = 10$ nm as well as other MFIM structures with $T_{FE} = 7$ and 5 nm. As shown in Figs. 2(a)–2(c), the simulated and experimental characteristics show a good agreement which validates the trends across different T_{FE} and applied voltages. The remarkable symmetry observed in the simulated characteristics in Figs. 2(a)–2(c) is a result of neglecting traps and defects in the phase-field simulation

framework along with the averaging over multiple voltage cycles which reduces the influence of stochastic nature of polarization switching.

We further calibrate the viscosity coefficient (Γ) of the TDGL equation for HZO by measuring the temporal evolution of polarization in MFIM capacitors as the dynamic experimental measurements for the MFIM stack were not available. We use the Positive-Up, Negative-Down (PUND) technique for this measurement with the experimental setup and pulse scheme described in Ref. 32 and reproduced in Figs. 2(d) and 2(e). The resulting evolution of simulated normalized polarization (P/P_s) shows a good match with experimental data³² [Fig. 2(f)]. For this study, we assume that the calibrated value of viscosity coefficient (Γ) using MFIM would still hold for the MFIM stack. The calibrated TDGL and material parameters for polycrystalline HZO-based MFIM stacks are summarized in Fig. 1(e).

III. DEVICE-TO-DEVICE VARIATIONS

In this section, we investigate the impact of applied voltage (V_{APP}) on the polycrystallinity-induced device-to-device variations in the MFIM stack. We further correlate the variations to the underlying polarization switching mechanisms and the multi-domain polarization profiles. Additionally, we analyze the effect of ferroelectric thickness (T_{FE}) on variations. To conduct this study, we employ a two-stage approach.

- **Stage-1:** We first use quasi-static simulations to study the variations by sweeping the applied voltage (V_{APP}) across the MFIM stack in small incremental steps and allowing samples to reach a steady state at each step. This stage enables us to understand the effect of maximum applied voltage [referred to as the set voltage (V_{SET})] on the variations decoupled from the time-dependent effects.
- **Stage-2:** We then use dynamic simulations to examine the impact of sharp voltage changes and the limited duration of voltage application on the variations, which is more representative of the typical use cases. Through this approach, we study the dependence of variations on the voltage pulse parameters, i.e., pulse amplitude (V_{pulse}) and pulse width (t_{pulse}).

In both stages of our study, we simulate 100 MFIM samples with a 3 nm Al_2O_3 interfacial layer and a 10 nm HZO ferroelectric layer unless otherwise specified. These samples are composed of different polycrystalline structures for the ferroelectric layer capturing variations in the number, size, shape, and orientation of the grains. To understand the dependencies of device-to-device variations, we focus on analyzing the distributions and the relevant statistical parameters especially the standard deviation [$\sigma(P_R)$] of remanent polarization (P_R) states across devices since P_R plays a central role in the distinguishability of memory states in FEFETs, FERAMs, and FTJs.

It is important to note that in addition to device-to-device variations, a single sample may exhibit variations in the device characteristics across multiple voltage cycles.²⁵ This is known as cycle-to-cycle variations or stochasticity and is primarily due to the stochastic nature of the domain nucleation. To minimize the effect of cycle-to-cycle variations in our analysis of device-to-device

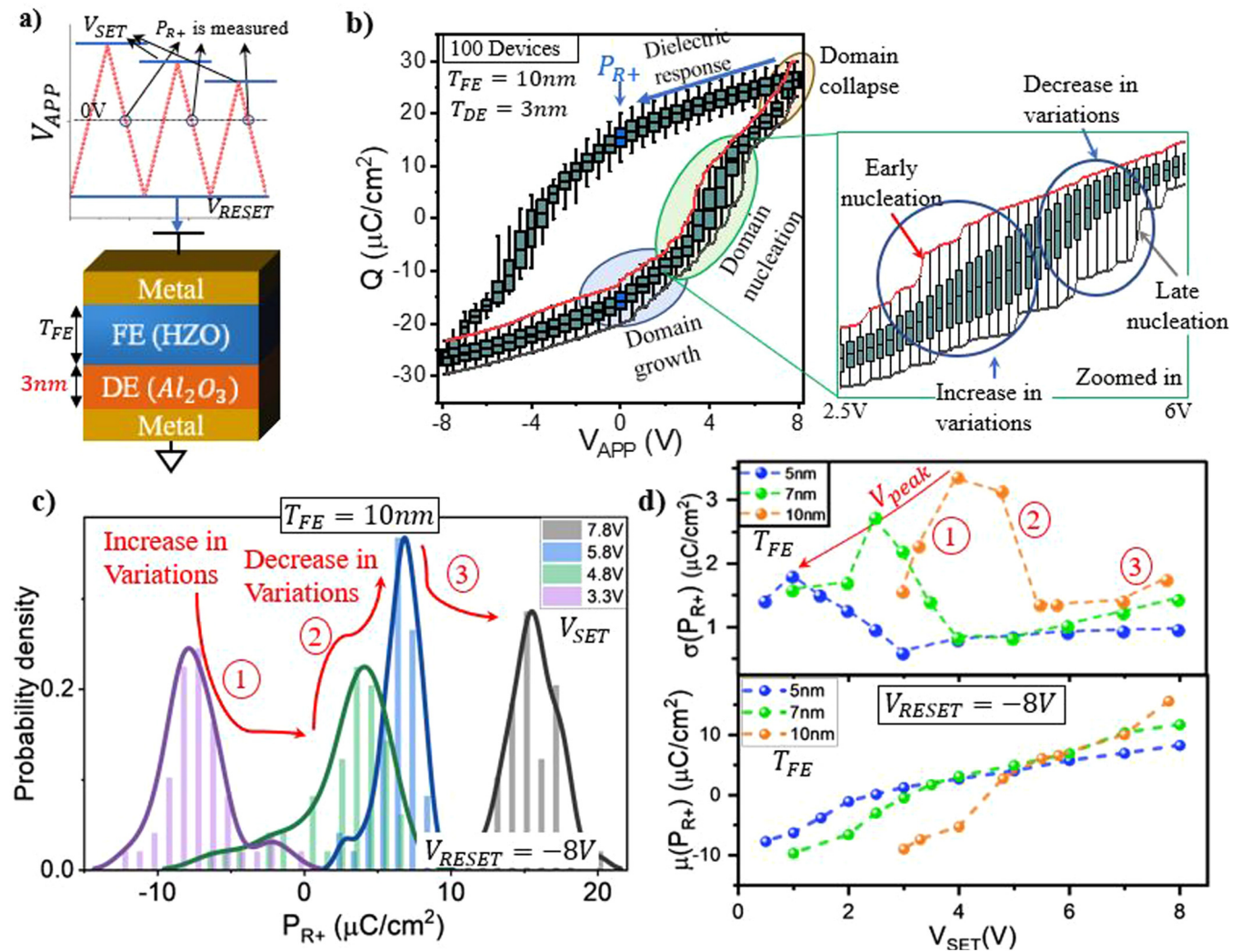
variations, the trends and results presented are averaged over five voltage cycles.

A. Quasi-static analysis

We begin by analyzing the impact of set voltage (V_{SET}) on variations by quasi-statically simulating the MFIM samples under a slowly varying V_{APP} [as in Fig. 3(a)]. The samples are simulated over a range of V_{SET} values while maintaining a fixed reset voltage (V_{RESET}) of -8 V . We specifically focus on the variations in the positive remanent polarization (P_{R+}), i.e., polarization at 0 V

during the backward path as V_{APP} decreases from V_{SET} [Figs. 3(a) and 3(b)].

The statistical distributions of P_{R+} for different V_{SET} values reveal a non-monotonic trend in the device-to-device variations as a function of V_{SET} [Fig. 3(c)]. The standard deviation of these variations [$\sigma(P_{R+})$] vs V_{SET} shown in Fig. 3(d) highlights this trend. As V_{SET} increases, an initial increase in the variations (labeled as region-1) is observed. This is followed by a decrease in $\sigma(P_{R+})$ (region-2) after V_{SET} surpasses a critical voltage (V_{peak}). As V_{SET} continues to increase, we see a slight increase in the variations again (region-3). It is worth pointing out that similar non-



30 October 2023 15:21:44

FIG. 3. (a) MFIM stack structure and the applied voltage (V_{APP}) pulse scheme of frequency 1 kHz used for quasi-static simulations. (b) Simulated Q - V_{APP} characteristics depicting the device-to-device variations at each voltage step (via box plot) with dominant polarization switching mechanisms highlighted, zoom in Q - V_{APP} highlighting the early and late nucleation across the samples. (c) Statistical distribution of variations in the simulated P_{R+} for different set voltages (V_{SET}) showing the non-monotonic dependence of variations. (d) Standard deviation [$\sigma(P_{R+})$] and mean [$\mu(P_{R+})$] of variations in simulated P_{R+} vs V_{SET} showing the non-monotonic trend in variations and the peak voltage (V_{peak}) for different FE thicknesses T_{FE} .

monotonic dependence of device-to-device variations on V_{SET} has been observed in experiments with HZO-based ferroelectric devices,^{23,28} albeit in a different structure.

Before we provide insight into the non-monotonic trends, let us briefly review the polarization-switching mechanisms in HZO. The polarization switching in HZO is primarily driven by two mechanisms: domain growth (domain-wall motion) and domain nucleation. When V_{APP} increases, domain growth-based switching leads to an increase in the size of existing $+P$ polarized domains. This results in a gradual change in polarization and smooth $Q-V_{APP}$ characteristics [see domain growth in Fig. 3(b)]. In contrast, domain nucleation involves the formation of new $+P$ polarized domains when the electric field in a region exceeds a critical value. This leads to an abrupt change in polarization and steep $Q-V_{APP}$ characteristics [see domain nucleation in Fig. 3(b)]. Notably, domain nucleation is a random process, dependent on the underlying polycrystalline structure as well as the multi-domain polarization and potential profiles.

To understand the mechanisms behind the non-monotonic trend, we will analyze the evolution of the underlying polarization domain profiles at the P_{R+} state as V_{SET} increases. Figure 4 shows the P_{R+} domain profiles as V_{SET} increases for two representative samples (sample-1 and sample-2). These samples are selected such that the sample-1 is around $+\sigma$ and sample-2 is around $-\sigma$ distance away from the mean of P_{R+} distribution for set voltage of 4.8 V (corresponding to maximum variations in P_{R+}). This choice is made so that the differences in the underlying polarization switching mechanisms and their dependence on polycrystalline structures can be clearly described and contrasted. Due to the variations in their underlying polycrystalline structures, the coercive voltage of sample-1 (V_{C1}) is lower than that of sample-2 (V_{C2}). Generalizing this observation to multiple samples, variations in the underlying polycrystalline structures lead to non-uniform

distribution of coercive voltage with a significant proportion of samples clustered around the mean.²⁵

As V_{SET} increases from 0V, the initial change in polarization is dominated by domain growth (until 3.3 V in Fig. 4), as the electric field in the FE layer is below the critical field required for nucleation. However, as V_{SET} continues to increase, the polarization switching in a small subset of samples transitions to domain nucleation (sample-1 between 3.3 and 4.8 V) as the electric field in these samples surpasses the critical threshold. This transition depends on various factors such as underlying polycrystalline structure and polarization domain profiles. This results in randomness in the polarization switching across the samples. The dominance of nucleation in this subset of samples leads to a sharp change in their polarization, while the majority of samples continue a gradual polarization change due to domain growth (sample-2 between 3.3 and 4.8 V). In other words, the increasing gap in polarization between the nucleating and non-nucleating samples start to widen the distribution of P_{R+} [increase in variations in Fig. 3(b)] and increase the device-to-device variations, as in region-1.

As V_{SET} continues to increase, two opposing effects come into picture. The larger number of domains in the early nucleating samples results in rapid change of polarization in these samples compared to the domain growth dominated ones. This tends to further increase the device-to-device variations. On the other hand, an increasing number of samples starts to nucleate with the increasing V_{SET} . These samples try to catch up the early nucleating ones striving to reduce the variations. But as long as the nucleation-driven samples are a minority compared to domain growth-dominated samples, the device-to-device variations continue to increase [as in region-1 in Figs. 3(c) and 3(d)] with V_{SET} . Therefore, this initial increase in variations with V_{SET} is mainly due to random domain nucleation and, in turn, the random but sharp

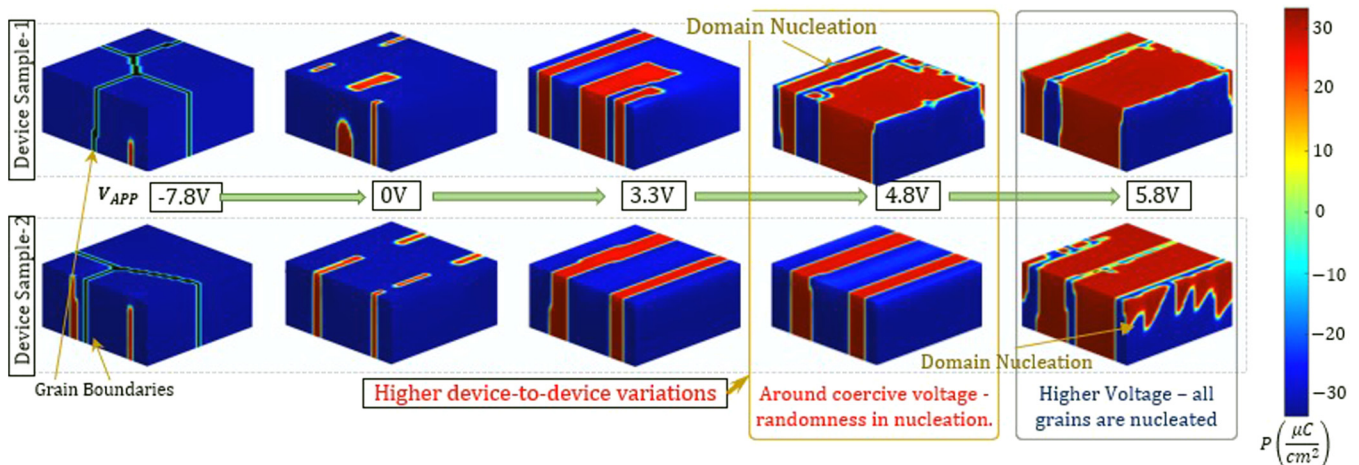


FIG. 4. Evolution of polarization domain profiles at the P_{R+} state in $20 \times 20 \times 10 \text{ nm}^3$ HZO samples (with the underlying polycrystalline structure embedded in the left most figure) starting from reset state with the increasing set voltage contrasting the underlying polarization switching mechanisms (domain growth and domain nucleation) and variations in two different samples.

30 October 2023 15:21:44

polarization change induced by it, which amplifies the variations in the underlying polycrystalline structures across the samples.

As V_{SET} increases beyond a critical voltage (V_{peak}), majority of samples transition to domain nucleation (e.g., sample-2 after 4.8 V in Fig. 4). Additionally, the early nucleating samples have already switched a significant amount of polarization, i.e., large areas of these samples switched to $+P$ domains (sample-1 after 4.8 V). This reduces the scope of further domain nucleation in these samples and causes them to transition back to domain growth. Domain growth leads to gradual polarization change in these samples, allowing the late nucleating samples to catch up. As a result, the distribution of polarization starts to narrow [labeled in Fig. 3(b)], reducing the device-to-device variations (as in region-2).

With further increase in V_{SET} , domain growth results in gradual expansion of $+P$ domains, while the oppositely polarized $-P$ domains shrink reaching a critical size. As a result, even a small increase in the applied voltage collapses these $-P$ domains—abruptly switching them to $+P$ regions. The point at which the domains collapse depends on the underlying polycrystalline structure and polarization domain profiles. Hence, this introduces a level of randomness in the switching behavior across the samples. Additionally, the collapse of domains switches a marginally higher polarization compared to pure domain growth. These two factors contribute to the slight increase in device-to-device variations as observed in region-3.

Interestingly, we observe that the non-monotonic trend in the variations with V_{SET} remains consistent across different FE thicknesses (T_{FE})—5, 7, and 10 nm [$\sigma(P_{R+})$ vs V_{SET} in Fig. 3(d)]. However, as T_{FE} decreases, we see a decrease in the maximum variations and a shift in the critical voltage (V_{peak}) to lower values. The reduction in the peak variations can be attributed to the evolution of denser domain patterns with T_{FE} scaling, resulting from the interplay between gradient and depolarization energies (details in Saha *et al.*²⁷). These denser domain patterns reduce the scope of domain nucleation, and domain growth becomes the dominant polarization-switching mechanism. Domain growth leads to gradual polarization switching, which, in turn, reduces the amplification of underlying polycrystalline variations. This results in the decrease of peak device-to-device variations with T_{FE} scaling. Further, the electric field in the FE layer surpasses the critical field required for nucleation at lower V_{SET} for scaled T_{FE} .²⁷ This results in the nucleation of new domains at lower V_{SET} and, in turn, the reduction of V_{peak} with T_{FE} scaling.

Although not explicitly shown here, we observe that reset voltage (V_{RESET}) has a similar impact on the device-to-device variations as the set voltage (V_{SET}), but with regard to the negative remanent polarization P_{R-} , which is associated with the reset state. This is attributed to the symmetry of the $Q-V_{APP}$ loops. In particular, we observe a non-monotonic trend in the variations of P_{R-} as V_{RESET} decreases from 0 V. This trend is characterized by an initial increase in the variations due to early nucleation of $-P$ domains in a small subset of samples, which amplifies the underlying polycrystalline variations. As V_{RESET} decreases and crosses the critical voltage, the variations decrease as most samples transition to domain nucleation and early nucleating samples shift to domain growth allowing the late nucleating ones to catch up. As V_{RESET} continues to decrease, the trend concludes with a slight increase in variations due to random collapse of $+P$ polarization domains.

B. Dynamic analysis

Next, we investigate the impact of voltage pulses on the device-to-device variations by dynamically simulating the MFIM samples with varying pulse amplitudes and widths [Fig. 5(a)]. To begin, we reset the samples by applying a reset pulse of -8 V for a prolonged duration—allowing the samples to reach a steady state. We then apply a sharp switching pulse with varying pulse widths (t_{pulse}) ranging from 2 to 100 ns and amplitudes (V_{pulse}) ranging from 4 to 10 V. After removing the switching pulse, we analyze the variations in the polarization state of the samples, which we refer to as the remanent polarization (P_{R+}). In particular, we investigate the impact of V_{pulse} and t_{pulse} on device-to-device variations in P_{R+} . We believe that the trends predicted by the phase-field simulation framework hold for the range of pulse widths considered (2–100 ns) as the viscosity coefficient (Γ), which determines the rate of polarization switching, is calibrated using high frequency measurements [Fig. 2(f)].

The results of our simulations reveal a significant dependence of variations in remanent polarization [$\sigma(P_{R+})$] on pulse width (t_{pulse}) and amplitude (V_{pulse}), as in Fig. 5(b). In particular, we observe that, for all pulse amplitudes, the variations are high initially and decrease with increasing pulse width [labeled as region-1 in Fig. 5(b)]. However, for pulse amplitudes ≤ 6 V, variations start to increase after certain pulse width [region-2a in Fig. 5(b)]. Whereas for higher amplitudes (of 8–10 V), variations continue to decrease as the pulse width increases [region-2b in Fig. 5(b)]. To better understand these trends, let us look at the underlying polarization domain profiles and correlate the variations to the effects of polycrystallinity and polarization switching mechanisms.

We begin by analyzing the initial decrease of variations in P_{R+} with increasing pulse width [region-1 in Fig. 5(b)]. The initially high variations observed at shorter t_{pulse} are primarily due to the polycrystallinity-induced variations in the switching times across the samples. To understand this, consider two grains with different orientation angles (θ_i). When subjected to voltage along the z axis, the grain with lower orientation angle experiences a stronger electric field [$E_z \cos(\theta_i)$] in the polarization direction. As a result, in accordance with Merz's law,³⁴ this grain with lower orientation angle responds faster than the one with the higher orientation angle.

When considering multiple samples, due to the variations in the underlying polycrystalline structures, some samples respond faster to the applied voltage pulse than the others. As a result, for the shorter pulse widths, these faster responding samples switch a large amount of polarization than the slower ones, leading to higher device-to-device variations. Additionally, the variations are observed to be higher for higher pulse amplitudes (V_{pulse}) as the higher V_{pulse} leads to dominance of domain nucleation due to the electric field in the FE layer crossing the critical threshold for nucleation [Fig. 5(d)] at 10 V at 3 ns. This leads to the switching of relatively large amount of polarization in the samples than lower V_{pulse} , which amplifies the underlying polycrystalline variations resulting in relatively higher device-to-device variations for higher V_{pulse} .

As the pulse width increases, the slower samples get adequate time to respond to the applied pulse. Additionally, the rate of

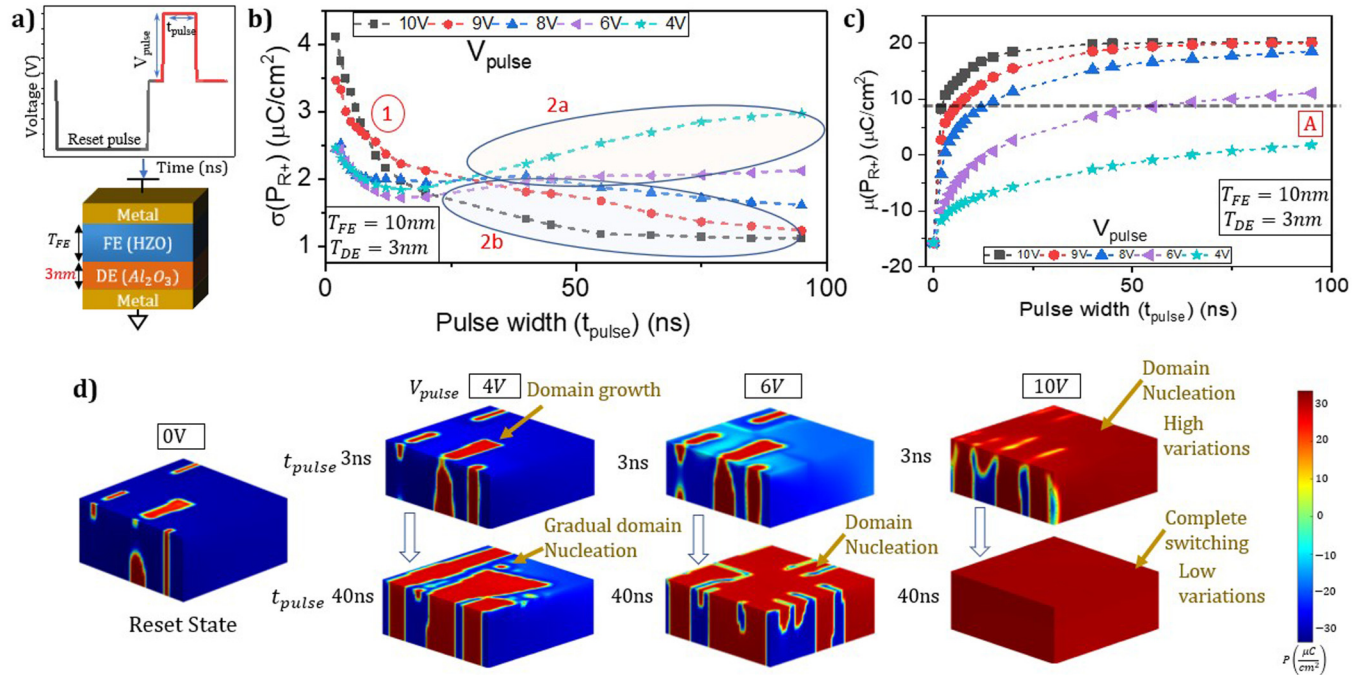


FIG. 5. (a) MFIM stack with the voltage pulse scheme used for dynamic analysis. (b) Standard deviation [$\sigma(P_{R+})$] and (c) mean [$\mu(P_{R+})$] of device-to-device variations vs pulse width (t_{pulse}) for different pulse amplitudes (V_{pulse}). (d) Polarization domain structures at reset state and V_{pulse} of 4, 6, and 10 V for t_{pulse} of 3 and 40 ns showing the difference in the underlying polarization switching schemes.

polarization change is typically more rapid at the onset of switching and gradually decreases as the switching progresses [$\mu(P_{R+})$ vs t_{pulse} in Fig. 5(c)]. As a result, the polarization switching in the faster responding samples slows down, allowing the slower samples to catch up and reducing the overall device-to-device variations. Furthermore, the decrease in variations with increasing pulse width is more pronounced for higher V_{pulse} due to the initial high variations. Moreover, higher V_{pulse} yields shorter switching times, which lead to a quicker response from the samples to the applied voltage. Therefore, at higher V_{pulse} , the slower responding samples catch up to the faster ones earlier compared to lower V_{pulse} . This results in pronounced reduction of the device-to-device variations with t_{pulse} for higher pulse amplitudes [region-1 in Fig. 5(b)].

As the pulse width increases further, we observe that the variations continue to decrease for higher V_{pulse} [10, 9, and 8 V in Fig. 5(b) region-2b]. This is because, at such high pulse amplitudes for long duration, the samples start to switch completely and reach a single domain state [Fig. 5(d), 10 V at 40 ns]. This results in the standard deviation of variations [$\sigma(P_{R+})$] saturating and being purely due to the polycrystallinity-induced variations in the grain shape and orientations (i.e., with minimal effect of multi-domain dynamics).

On the other hand, for lower pulse amplitudes [≤ 6 V in Fig. 5(b) region-2a], we see that the variations start to increase after a certain pulse width. The increase in variations is due to the onset of domain nucleation [Fig. 5(d), 6 and 4 V at 40 ns]. Even though

the pulse amplitude is constant, the evolution of underlying domain structures causes the onset of nucleation with increasing t_{pulse} . In the multi-domain scenario, the field lines from the $+P$ domains terminate in $-P$ domains around the domain walls.²⁷ These fields, known as the stray fields, help reduce the depolarization field in the FE layer. However, as the $+P$ regions grow due to domain growth at low pulse widths [Fig. 5(d), 4 and 6 V at 3 ns] and come close to each other, the stray fields accumulate in the intermediate $-P$ region from both the $+P$ domains. This accumulation of stray fields causes the total electric field in the region to exceed the nucleation critical threshold and initiates the nucleation of new $+P$ domains. For the pulse amplitudes falling in the range of coercive voltage distribution across the samples (for example, 4 V), domain nucleation occurs only in a subset of samples, which exacerbates the increase in variations.

Furthermore, certain applications such as multi-state memories, synapses require achieving a partially switched (intermediate) polarization state across samples. The plot of the mean of P_{R+} across samples vs pulse width [$\mu(P_{R+})$ vs t_{pulse} in Fig. 5(c)] indicates the possibility of reaching this target polarization state via various appropriate combinations of pulse widths and amplitudes. By “appropriate combinations,” we mean that one can use either a higher amplitude pulse for shorter duration or a lower amplitude pulse for longer duration, as long as the pulse amplitude exceeds a certain threshold such that the target polarization state can be reached. However, it is important to note that the device-to-device

30 October 2023 15:21:44

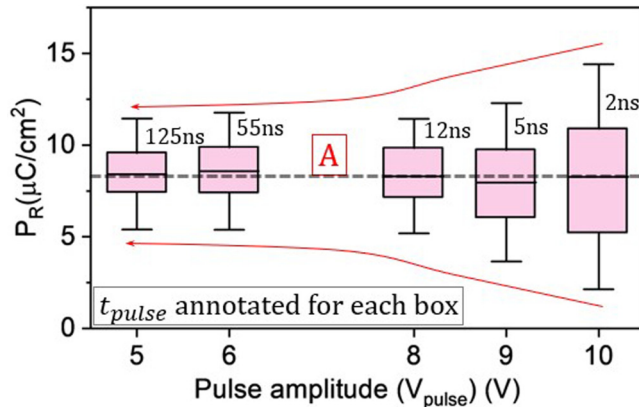


FIG. 6. Box plots of P_{R+} across the samples showing the variations and the pulse width required for different pulse amplitudes to reach the target mean partially switched polarization state (A).

variations associated with these pulse combinations can be quite different and understanding the dependence of the variations on the pulse combinations play a crucial role in optimizing the devices.

Therefore, we consider one such representative state [labeled as A in Fig. 5(c)] and analyze the variations associated with different pulse combinations that can be used to reach this state A. Our results (Fig. 6) indicate that while the final mean polarization is similar, the resulting device-to-device variations vary across these combinations. In particular, we find that using lower amplitude pulses for longer duration results in lower variations across samples compared to using higher pulses for shorter duration.

This is because, when using a higher amplitude pulse for a shorter duration, the underlying variations in the switching time across the samples come into play. The fast-responding samples switch a significant amount of polarization (due to higher V_{pulse}) while the slow ones may not completely respond to the applied pulse. This leads to larger device-to-device variations. On the other hand, when using lower amplitude pulses for a longer duration, the variations in the switching times do not affect significantly as slow samples get more time to respond to the applied pulse. This results in reducing the overall device-to-device variations.

However, it should be noted that a decrease in pulse amplitude beyond a certain point yield diminishing returns, i.e., we see little to no reduction in variations. Additionally, using lower amplitude pulses also comes with a trade-off as the pulse widths necessary to reach the target state increase drastically with decreasing pulse amplitudes. Therefore, to counter the device-to-device variations in P_{R+} , reducing the pulse amplitude along with increasing the pulse width can be appealing but only up till a point beyond which the latency costs drastically increase with minimal improvement in variations.

IV. SUMMARY

We analyzed the effect of applied voltage on the polycrystalline-induced device-to-device variations in HZO-based MFIM stacks. Based on 3D multi-grain phase-field simulations, we

showed a non-monotonic dependence of variations on the set voltage, which is in good agreement with previous experiments. We correlated this trend in variations to the underlying polarization switching mechanisms and the collapse of domains. Furthermore, we analyzed the impact of ferroelectric thickness scaling and discussed its utility in reducing the peak variations. Additionally, we analyzed the dependence of variations on voltage pulse parameters such as pulse width and amplitude. We demonstrated that for multi-state operation, when aiming for an intermediate or partially switched polarization state, using a lower amplitude pulse for longer duration results in reduced variations compared to a higher amplitude pulse for a shorter duration.

ACKNOWLEDGMENTS

This work was supported by the Semiconductor Research Corporation (SRC) under Contract No. 2020-LM-2959 and the National Science Foundation (NSF) under Grant No. 2008412.

AUTHOR DECLARATIONS

Conflict of Interest

The authors have no conflicts to disclose.

Author Contributions

Revant Koduru: Conceptualization (equal); Data curation (equal); Formal analysis (equal); Investigation (equal); Methodology (equal); Software (equal); Visualization (equal); Writing – original draft (equal); Writing – review & editing (equal). **Imtiaz Ahmed:** Data curation (equal); Formal analysis (equal); Methodology (equal); Software (equal); Visualization (equal). **Atanu K. Saha:** Conceptualization (equal); Investigation (equal); Methodology (equal); Software (equal); Writing – review & editing (equal). **Xiao Lyu:** Data curation (equal); Investigation (equal); Methodology (equal); Resources (equal). **Peide Ye:** Conceptualization (equal); Investigation (equal); Resources (equal); Supervision (equal); Writing – original draft (equal). **Sumeet K. Gupta:** Conceptualization (equal); Funding acquisition (equal); Investigation (equal); Methodology (equal); Supervision (equal); Validation (equal); Writing – original draft (equal); Writing – review & editing (equal).

DATA AVAILABILITY

The data that support the findings of this study are available from the corresponding author upon reasonable request.

REFERENCES

- T. S. Böscke, J. Müller, D. Bräuhaus, U. Schröder, and U. Böttger, “Ferroelectricity in hafnium oxide thin films,” *Appl. Phys. Lett.* **99**, 102903 (2011).
- J. Müller, T. S. Böscke, S. Müller, E. Yurchuk, P. Polakowski, J. Paul, D. Martin, T. Schenk, K. Khullar, A. Kersch, W. Weinreich, S. Riedel, K. Seidel, A. Kumar, T. M. Arruda, S. V. Kalinin, T. Schlosser, R. Boschke, R. Van Bentum, U. Schroder, and T. Mikolajick, “Ferroelectric hafnium oxide: A CMOS-compatible and highly scalable approach to future ferroelectric memories,” in *2013 IEEE International Electron Devices Meeting (IEEE, Washington, DC, 2013)*, pp. 10.8.1–10.8.4.

- ³H.-J. Lee, M. Lee, K. Lee, J. Jo, H. Yang, Y. Kim, S. C. Chae, U. Waghmare, and J. H. Lee, "Scale-free ferroelectricity induced by flat phonon bands in HfO_2 ," *Science* **369**, 1343–1347 (2020).
- ⁴H. Mulaosmanovic, T. Mikolajick, and S. Slesazek, "Accumulative polarization reversal in nanoscale ferroelectric transistors," *ACS Appl. Mater. Interfaces* **10**, 23997–24002 (2018).
- ⁵A. K. Saha, K. Ni, S. Dutta, S. Datta, and S. Gupta, "Phase field modeling of domain dynamics and polarization accumulation in ferroelectric HZO," *Appl. Phys. Lett.* **114**, 202903 (2019).
- ⁶T. Ali, K. Kuhnel, M. Czernohorsky, C. Mart, M. Rudolph, B. Patzold, M. Lederer, R. Olivo, D. Lehninger, F. Muller, R. Hoffmann, J. Metzger, R. Binder, P. Steinke, T. Kampfe, J. Muller, K. Seidel, and L. M. Eng, "A study on the temperature-dependent operation of fluorite-structure-based ferroelectric HfO_2 memory FeFET: A temperature-modulated operation," *IEEE Trans. Electron Devices* **67**, 2793–2799 (2020).
- ⁷M. Hoffmann, M. Pešić, K. Chatterjee, A. I. Khan, S. Salahuddin, S. Slesazek, U. Schroeder, and T. Mikolajick, "Direct observation of negative capacitance in polycrystalline ferroelectric HfO_2 ," *Adv. Funct. Mater.* **26**, 8643–8649 (2016).
- ⁸D.-H. Choe, S. Kim, T. Moon, S. Jo, H. Bae, S.-G. Nam, Y. S. Lee, and J. Heo, "Unexpectedly low barrier of ferroelectric switching in HfO_2 via topological domain walls," *Mater. Today* **50**, 8–15 (2021).
- ⁹A. K. Saha and S. K. Gupta, "Multi-domain ferroelectric FETs with negative and enhanced positive capacitance for logic applications," in *2021 International Conference on Simulation of Semiconductor Processes and Devices (SISPAD)* (IEEE, Dallas, TX, 2021), pp. 77–80.
- ¹⁰J. Muller, E. Yurchuk, T. Schlosser, J. Paul, R. Hoffmann, S. Muller, D. Martin, S. Slesazek, P. Polakowski, J. Sundqvist, M. Czernohorsky, K. Seidel, P. Kucher, R. Boschke, M. Trentzsch, K. Gebauer, U. Schroeder, and T. Mikolajick, "Ferroelectricity in HfO_2 enables nonvolatile data storage in 28 nm HKMGm," in *2012 Symposium on VLSI Technology (VLSIT)* (IEEE, Honolulu, HI, 2012), pp. 25–26.
- ¹¹K. Ni, B. Grisafe, W. Chakraborty, A. K. Saha, S. Dutta, M. Jerry, J. A. Smith, S. Gupta, and S. Datta, "In-memory computing primitive for sensor data fusion in 28 nm HKMG FeFET technology," in *2018 IEEE International Electron Devices Meeting (IEDM)* (IEEE, San Francisco, CA, 2018), pp. 16.1.1–16.1.4.
- ¹²M. Jerry, S. Dutta, A. Kazemi, K. Ni, J. Zhang, P.-Y. Chen, P. Sharma, S. Yu, X. S. Hu, M. Niemier, and S. Datta, "A ferroelectric field effect transistor based synaptic weight cell," *J. Phys. D: Appl. Phys.* **51**, 434001 (2018).
- ¹³S. Dutta, A. Saha, P. Panda, W. Chakraborty, J. Gomez, A. Khanna, S. Gupta, K. Roy, and S. Datta, "Biologically plausible ferroelectric quasi-leaky integrate and fire neuron," in *2019 Symposium on VLSI Technology* (IEEE, Kyoto, 2019), pp. T140–T141.
- ¹⁴U. Schroeder, M. H. Park, T. Mikolajick, and C. S. Hwang, "The fundamentals and applications of ferroelectric HfO_2 ," *Nat. Rev. Mater.* **7**, 653–669 (2022).
- ¹⁵N. Tasneem, Z. Wang, Z. Zhao, N. Upadhyay, S. Lombardo, H. Chen, J. Hur, D. Triyoso, S. Consiglio, K. Tapily, R. Clark, G. Leusink, S. Kurinec, S. Datta, S. Yu, K. Ni, M. Passlack, W. Chern, and A. Khan, "Trap capture and emission dynamics in ferroelectric field-effect transistors and their impact on device operation and reliability," in *2021 IEEE International Electron Devices Meeting (IEDM)* (IEEE, San Francisco, CA, 2021), pp. 6.1.1–6.1.4.
- ¹⁶M. Trentzsch, S. Flachowsky, R. Richter, J. Paul, B. Reimer, D. Utess, S. Jansen, H. Mulaosmanovic, S. Muller, S. Slesazek, J. Ocker, M. Noack, J. Muller, P. Polakowski, J. Schreiber, S. Beyer, T. Mikolajick, and B. Rice, "A 28 nm HKMG super low power embedded NVM technology based on ferroelectric FETs," in *2016 IEEE International Electron Devices Meeting (IEDM)* (IEEE, San Francisco, CA, 2016), pp. 11.5.1–11.5.4.
- ¹⁷Z. Wang, M. M. Islam, P. Wang, S. Deng, S. Yu, A. I. Khan, and K. Ni, "Depolarization field induced instability of polarization states in HfO_2 based ferroelectric FET," in *2020 IEEE International Electron Devices Meeting (IEDM)* (IEEE, San Francisco, CA, 2020), pp. 4.5.1–4.5.4.
- ¹⁸P. Sharma, K. Tapily, A. K. Saha, J. Zhang, A. Shaughnessy, A. Aziz, G. L. Snider, S. Gupta, R. D. Clark, and S. Datta, "Impact of total and partial dipole switching on the switching slope of gate-last negative capacitance FETs with ferroelectric hafnium zirconium oxide gate stack," in *2017 Symposium on VLSI Technology* (IEEE, Kyoto, 2017), pp. T154–T155.
- ¹⁹M. Pesic, B. Beltrando, A. Padovani, S. Gangopadhyay, M. Kaliappan, M. Haverty, M. A. Villena, E. Piccinini, M. Bertocchi, T. Chiang, L. Larcher, J. Strand, and A. L. Shluger, "Variability sources and reliability of 3D-FeFETs," in *2021 IEEE International Reliability Physics Symposium (IRPS)* (IEEE, Monterey, CA, 2021), pp. 1–7.
- ²⁰M. Pesic and B. Beltrando, "Embedding ferroelectric HfO_x in memory hierarchy: Material—defects—device entanglement," in *2021 IEEE International Electron Devices Meeting (IEDM)* (IEEE, San Francisco, CA, 2021), pp. 33.4.1–33.4.4.
- ²¹K. Ni, W. Chakraborty, J. Smith, B. Grisafe, and S. Datta, "Fundamental understanding and control of device-to-device variation in deeply scaled ferroelectric FETs," in *2019 Symposium on VLSI Technology* (IEEE, Kyoto, 2019), pp. T40–T41.
- ²²S. Dunkel, M. Trentzsch, R. Richter, P. Moll, C. Fuchs, O. Gehring, M. Majer, S. Wittek, B. Muller, T. Melde, H. Mulaosmanovic, S. Slesazek, S. Muller, J. Ocker, M. Noack, D.-A. Lohr, P. Polakowski, J. Muller, T. Mikolajick, J. Hontschel, B. Rice, J. Pellerin, and S. Beyer, "A FeFET based super-low-power ultra-fast embedded NVM technology for 22 nm FDSOI and beyond," in *2017 IEEE International Electron Devices Meeting (IEDM)* (IEEE, San Francisco, CA, 2017), pp. 19.7.1–19.7.4.
- ²³K. Chatterjee, S. Kim, G. Karbasian, D. Kwon, A. J. Tan, A. K. Yadav, C. R. Serrao, C. Hu, and S. Salahuddin, "Challenges to partial switching of $\text{Hf}_{0.8}\text{Zr}_{0.2}\text{O}_2$ gated ferroelectric FET for multilevel/analog or low-voltage memory operation," *IEEE Electron Device Lett.* **40**, 1423–1426 (2019).
- ²⁴K. Ni, A. Gupta, O. Prakash, S. Thomann, X. S. Hu, and H. Amrouch, "Impact of extrinsic variation sources on the device-to-device variation in ferroelectric FET," in *2020 IEEE International Reliability Physics Symposium (IRPS)* (IEEE, Dallas, TX, 2020), pp. 1–5.
- ²⁵R. Koduru, A. K. Saha, M. Si, X. Lyu, P. D. Ye, and S. K. Gupta, "Variation and stochasticity in polycrystalline HZO based MFIM: Grain-growth coupled 3D phase field model based analysis," in *2021 IEEE International Electron Devices Meeting (IEDM)* (IEEE, San Francisco, CA, 2021), pp. 15.2.1–15.2.4.
- ²⁶J. Müller, T. S. Böscke, U. Schröder, S. Mueller, D. Bräuhäus, U. Böttger, L. Frey, and T. Mikolajick, "Ferroelectricity in simple binary ZrO_2 and HfO_2 ," *Nano Lett.* **12**, 4318–4323 (2012).
- ²⁷A. K. Saha, M. Si, K. Ni, S. Datta, P. D. Ye, and S. K. Gupta, "Ferroelectric thickness dependent domain interactions in FEFETs for memory and logic: A phase-field model based analysis," in *2020 IEEE International Electron Devices Meeting (IEDM)* (IEEE, San Francisco, CA, 2020), pp. 4.3.1–4.3.4.
- ²⁸T. Ali, P. Polakowski, K. Kuhnel, M. Czernohorsky, T. Kampfe, M. Rudolph, B. Patzold, D. Lehninger, F. Muller, R. Olivo, M. Lederer, R. Hoffmann, P. Steinke, K. Zimmermann, U. Muhle, K. Seidel, and J. Muller, "A multilevel FeFET memory device based on laminated HSO and HZO ferroelectric layers for high-density storage," in *2019 IEEE International Electron Devices Meeting (IEDM)* (IEEE, San Francisco, CA, 2019), pp. 28.7.1–28.7.4.
- ²⁹C. Krill III and L.-Q. Chen, "Computer simulation of 3-D grain growth using a phase-field model," *Acta Mater.* **50**, 3059–3075 (2002).
- ³⁰M. H. Park, Y. H. Lee, H. J. Kim, T. Schenk, W. Lee, K. D. Kim, F. P. G. Fengler, T. Mikolajick, U. Schroeder, and C. S. Hwang, "Surface and grain boundary energy as the key enabler of ferroelectricity in nanoscale hafnia-zirconia: A comparison of model and experiment," *Nanoscale* **9**, 9973–9986 (2017).
- ³¹M. Hyuk Park, H. Joon Kim, Y. Jin Kim, W. Lee, T. Moon, and C. Seong Hwang, "Evolution of phases and ferroelectric properties of thin $\text{Hf}_{0.5}\text{Zr}_{0.5}\text{O}_2$ films according to the thickness and annealing temperature," *Appl. Phys. Lett.* **102**, 242905 (2013).
- ³²X. Lyu, M. Si, P. R. Shrestha, K. P. Cheung, and P. D. Ye, "Dynamics studies of polarization switching in ferroelectric hafnium zirconium oxide," in *2021 5th IEEE Electron Devices Technology and Manufacturing Conference (EDTM)* (IEEE, Chengdu, 2021), pp. 1–3.
- ³³A. K. Saha, M. Si, P. D. Ye, and S. K. Gupta, "Polarization switching in $\text{Hf}_{0.5}\text{Zr}_{0.5}\text{O}_2$ -dielectric stack: The role of dielectric layer thickness," *Appl. Phys. Lett.* **119**, 122903 (2021).
- ³⁴W. J. Merz, "Domain formation and domain wall motions in ferroelectric BaTiO_3 single crystals," *Phys. Rev.* **95**, 690–698 (1954).